

## Critical turbidity thresholds for maintenance of estuarine tidal flats worldwide

Grandjean, Tim J.; Weenink, Roland; van der Wal, Daphne; Addink, Elisabeth A.; Hu, Zhan; Liu, Shuai; Wang, Zheng B.; Lin, Yuan; Bouma, Tjeerd J.

**DOI**

[10.1038/s41561-024-01431-3](https://doi.org/10.1038/s41561-024-01431-3)

**Publication date**

2024

**Document Version**

Final published version

**Published in**

Nature Geoscience

**Citation (APA)**

Grandjean, T. J., Weenink, R., van der Wal, D., Addink, E. A., Hu, Z., Liu, S., Wang, Z. B., Lin, Y., & Bouma, T. J. (2024). Critical turbidity thresholds for maintenance of estuarine tidal flats worldwide. *Nature Geoscience*, 17(6), 539-544. <https://doi.org/10.1038/s41561-024-01431-3>

**Important note**

To cite this publication, please use the final published version (if applicable).  
Please check the document version above.

**Copyright**

Other than for strictly personal use, it is not permitted to download, forward or distribute the text or part of it, without the consent of the author(s) and/or copyright holder(s), unless the work is under an open content license such as Creative Commons.

**Takedown policy**

Please contact us and provide details if you believe this document breaches copyrights.  
We will remove access to the work immediately and investigate your claim.

***Green Open Access added to TU Delft Institutional Repository***

***'You share, we take care!' - Taverne project***

**<https://www.openaccess.nl/en/you-share-we-take-care>**

Otherwise as indicated in the copyright section: the publisher is the copyright holder of this work and the author uses the Dutch legislation to make this work public.

# Critical turbidity thresholds for maintenance of estuarine tidal flats worldwide

Received: 30 June 2023

Accepted: 21 March 2024

Published online: 06 May 2024

 Check for updates

Tim J. Grandjean <sup>1,2</sup>✉, Roland Weenink <sup>1,3</sup>, Daphne van der Wal <sup>1,4</sup>, Elisabeth A. Addink <sup>2</sup>, Zhan Hu <sup>5,6,7</sup>, Shuai Liu <sup>5</sup>, Zheng B. Wang <sup>8,9</sup>, Yuan Lin <sup>10,11</sup> & Tjeerd J. Bouma<sup>1,2</sup>

Tidal flats are shrinking in extent globally. The dynamics of the response of estuarine tidal flats to global environmental changes remain unclear. Tidal-flat morphology is shaped by the interplay among wave and tidal forces, river discharge and sediment supply, and preservation of tidal flats requires a balance between erosional and depositional processes be maintained. Here we assess tidal-flat morphodynamic changes of 40 globally distributed estuaries with contrasting tidal amplitudes between 1986 and 2011 from analyses of 4,939 satellite images. We consider both vegetated and unvegetated intertidal areas. From comparisons with remote-sensing-derived turbidity estimates, we identify a critical turbidity threshold indicative of a minimum sediment supply along with the hydrodynamic forces, which is necessary to maintain tidal flats. Tidal flats in intertidal areas in estuaries with low turbidity face retreat, with the critical turbidity threshold increasing with increasing tidal amplitudes. By contrast, estuaries with high turbidity tend to exhibit laterally or vertically expanding tidal flats. However, despite estuaries with limited tidal ranges having relatively low turbidity thresholds, environmental or anthropogenic alterations can still adversely affect the morphology of tidal flats. Our findings demonstrate the need to consider sediment supply in integrated estuarine management strategies to maintain the ecological integrity and flood defence function of tidal flats.

Globally, more than one billion people live in or near deltas and estuaries and face exposure to sea-level rise (SLR)<sup>1,2</sup>. These communities benefit from and depend on crucial coastal ecosystem services provided by intertidal ecosystems<sup>3</sup>, such as food provision<sup>4</sup>, shoreline stabilization<sup>5</sup> and flood protection<sup>6</sup>. Flood protection is especially

provided by vegetation in the high intertidal range, such as salt marshes and mangroves<sup>7–9</sup>. To address SLR, adopting ecosystem-based flood defences offers a sustainable and economically efficient solution compared with traditional coastal engineering methods such as sea walls and dykes, ensuring protection for coastal communities<sup>6</sup>; hence, the

<sup>1</sup>Department of Estuarine and Delta Systems, Royal Netherlands Institute for Sea Research (NIOZ), Yerseke, the Netherlands. <sup>2</sup>Faculty of Geosciences, Department of Physical Geography, Utrecht University, Utrecht, the Netherlands. <sup>3</sup>Faculty of Science, Utrecht University, Utrecht, the Netherlands. <sup>4</sup>Faculty of Geo-Information Science and Earth Observation (ITC), University of Twente, Enschede, the Netherlands. <sup>5</sup>School of Marine Sciences, Sun Yat-Sen University and Southern Marine Science and Engineering Guangdong Laboratory (Zhuhai), Zhuhai, China. <sup>6</sup>Guangdong Provincial Key Laboratory of Marine Resources and Coastal Engineering, Guangzhou, China. <sup>7</sup>Pearl River Estuary Marine Ecosystem Research Station, Ministry of Education, Zhuhai, China. <sup>8</sup>Faculty of Civil Engineering and Geosciences, Delft University of Technology, Delft, the Netherlands. <sup>9</sup>Deltares, Delft, the Netherlands. <sup>10</sup>State Key Laboratory of Estuarine and Coastal Research, Institute of Eco-Chongming, Center for Blue Carbon Science and Technology, East China Normal University, Shanghai, China. <sup>11</sup>Yangtze Delta Estuarine Wetland Ecosystem Observation and Research Station, Shanghai, China. ✉e-mail: [tim.grandjean@nioz.nl](mailto:tim.grandjean@nioz.nl)

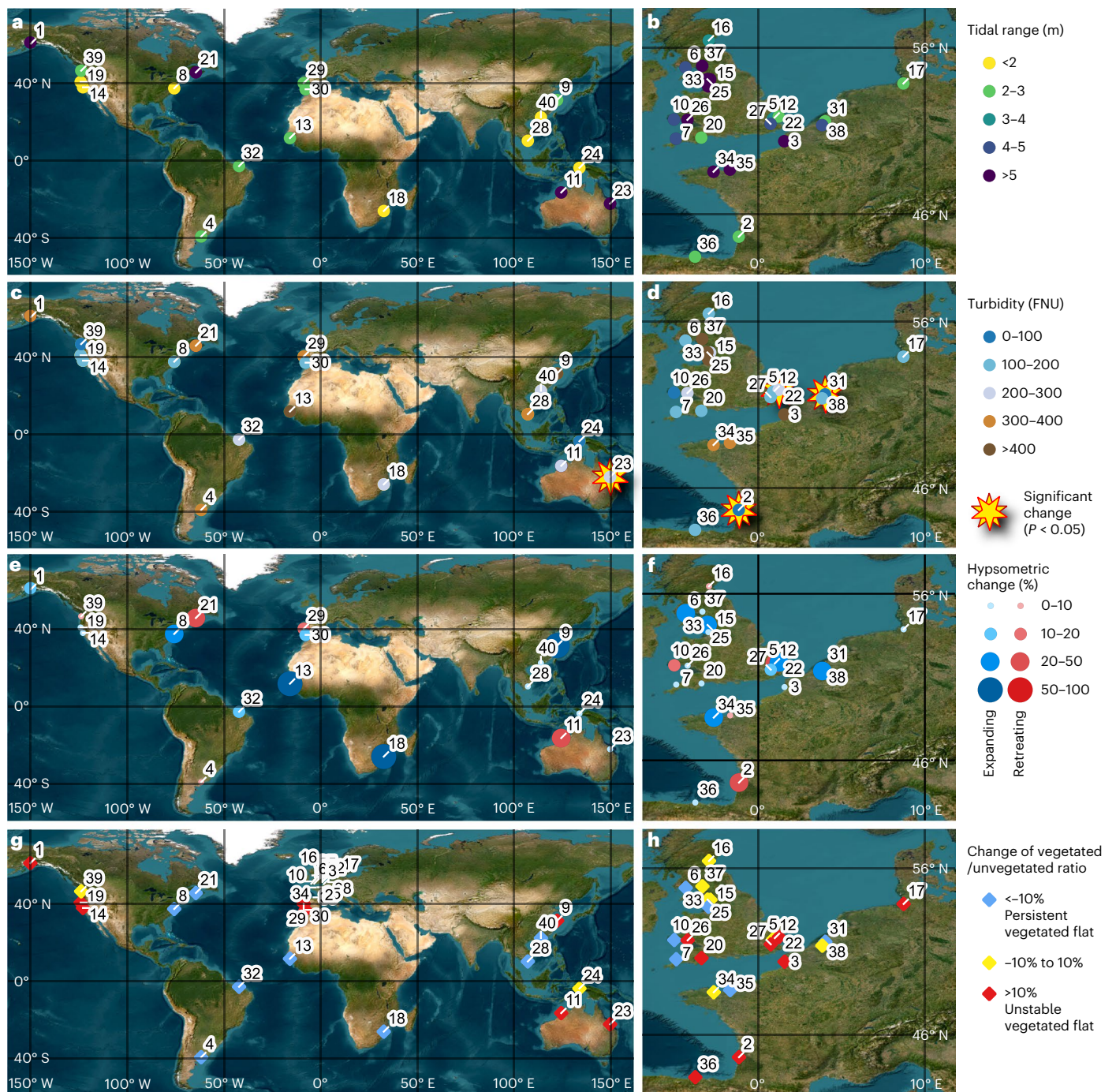


**Fig. 1 | Spatial distributions of estuaries, environmental characteristics and morphological trajectories.** **a, b**, Estuaries categorized by tidal range, with light colours for micro-tidal and meso-tidal regimes (**a**) and dark colours for macro-tidal regimes (**b**). **c, d**, Turbidity levels from 2009 to 2011 and trends from 1986 to 2011, using blue for low turbidity (**c**) and brown for high turbidity (**d**), with significant changes marked by stars. **e, f**, Morphological changes in tidal flats

from the period 1986–1988 to 2009–2011, where red dots represent retreating flats (**e**) and blue dots expanding flats (**f**). **g, h**, Changes in vegetated intertidal areas, with red diamonds for loss in vegetation proportion (**g**), blue for gain in vegetation proportion and yellow for stable vegetation proportion (**h**). Credit: basemaps, Esri, Maxar, Earthstar Geographics and the GIS User Community ([http://goto.arcgisonline.com/maps/World\\_Imagery](http://goto.arcgisonline.com/maps/World_Imagery)).

responses of intertidal marshes and mangroves to SLR and changes in sediment concentrations have been widely studied<sup>10–12</sup>. Plants in salt marshes and mangroves effectively trap sediment and promote accretion, even under declining sediment supply and SLR<sup>13,14</sup>. However, for marshes and mangroves to maintain their lateral width, especially when landward expansion is constrained, it is essential to preserve the unvegetated tidal flats that front the vegetation at its seaward side<sup>15–17</sup>. The responses of unvegetated tidal flats to SLR and reduced sediment supply have received little attention, although the global distribution

of tidal flats declined by an estimated 16% between 1984 and 2016<sup>18</sup>. It is thought that this decline and anticipated future losses due to accelerated SLR may be related to a diminishing sediment supply caused by human activities, such as damming, irrigating and improving land-use practices<sup>19–21</sup>. Reduced fluvial sediment supply has been proved to induce erosion of tidal flats that front salt marshes<sup>22</sup>. However, global assessments that specifically address whether and how diminished sediment supply impacts the morphology of unvegetated tidal flats remain scarce.

Recent advances in high-performance computing regarding Earth's observational data have allowed for an increase in the number of studies concerning the lateral extent of tidal flats globally<sup>18,23</sup>, the morphology of tidal flats on local scales<sup>24</sup> and the retrieval of turbidity data from satellite imagery<sup>25</sup>, all of which provide valuable insights into the dynamics of coastal ecosystems at different scales. Despite these advances, our understanding of how environmental factors affect the morphology of tidal flats on a global scale, particularly the combined effects of tidal amplitudes and sediment supply, has not been thoroughly explored. We applied both the waterline extraction method, which uses satellite imagery to create interpolated digital elevation models (DEMs) of tidal flats<sup>24</sup>, and the unsupervised salt-marsh classification procedure<sup>26</sup> to study the morphological development (changes in intertidal volume as well as lateral and vertical extents) of 40 estuarine tidal flats worldwide between 1986 and 2011. Our analysis linked this morphological development of tidal flats to local turbidity levels derived from remotely sensed data. Through our study, we found a critical turbidity threshold (CTT), which emerges as an important parameter for the existence of tidal flats and for the distinction of systems with overall loss and expansion of tidal flats, respectively. Recognizing this relationship is instrumental in enhancing sediment management and restoring intertidal systems.

### Changing environmental conditions

Globally, tidal-flat morphology exhibits distinctive characteristics across different tidal ranges, from micro-tidal (<2 m) and meso-tidal (2–4 m) to macro-tidal (>4 m) systems<sup>27</sup>. In general, the morphology of tidal flats is directly impacted by a combination of tidal dynamics coupled with the local wave climates, river discharge and sediment supply<sup>28</sup>. In the upcoming decades, however, both projected SLR and anthropogenic disturbances are expected to alter tidal amplitudes in estuaries and indirectly impact the morphodynamics<sup>29</sup>. Furthermore, the continuous supply of sediment, essential for the sustenance and stability of tidal flats, is threatened due to worldwide changes in watershed alterations<sup>19,21,30,31</sup> and storm-induced dynamics<sup>32,33</sup>. Alterations in sediment supply, or turbidity as an indicator of sediment supply<sup>34,35</sup> measured in formazin nephelometric units (FNU), are assumed to have critical implications for the future morphology of tidal flats, although the impact remains to be fully elucidated.

Our study examined 40 estuaries covering a wide range of tidal amplitudes, from micro-tidal (1.19 m) to macro-tidal (8.96 m) (Fig. 1a,b and Supplementary Table 1). We observed significant changes in turbidity for 10% (4) of the estuaries between the periods 1986–1988 and 2009–2011 (Fig. 1c,d and Supplementary Table 1); specifically, 5% (2) show a decrease and the other 5% (2) an increase in turbidity. In 90% (36) of the estuaries, our analysis did not reveal significant changes in turbidity over the two studied periods. These findings suggest that, overall, there is no strong trend observed in turbidity changes across the studied estuaries. Turbidity is subject to substantial spatial and temporal variability, influenced by factors such as wave-induced sediment resuspension<sup>32,35</sup>, periodic variations in the spring-neap cycle<sup>36</sup> and seasonal cycles of wet or dry and calm or stormy periods<sup>37</sup>. Despite this constraint, our approach effectively classified differences among estuaries, which is crucial for identifying specific turbidity thresholds despite the absence of trends in the majority.

### Intertidal morphological developments

The global analysis conducted in this study, using hypsometric curves to monitor changes in intertidal topography between the periods 1986–1988 and 2009–2011, shows that 25% (10) of the 40 studied estuaries experienced a decline in their overall tidal-flat elevation (vertical dimension) or extent (lateral dimension), or both, while the remaining 75% (30) exhibited expansion in one or both dimensions (Fig. 1e,f and Extended Data Fig. 1). Of the studied estuaries, 55% (22) are along the west coast of Europe; 32% (7) of these experienced a decline in their elevation and

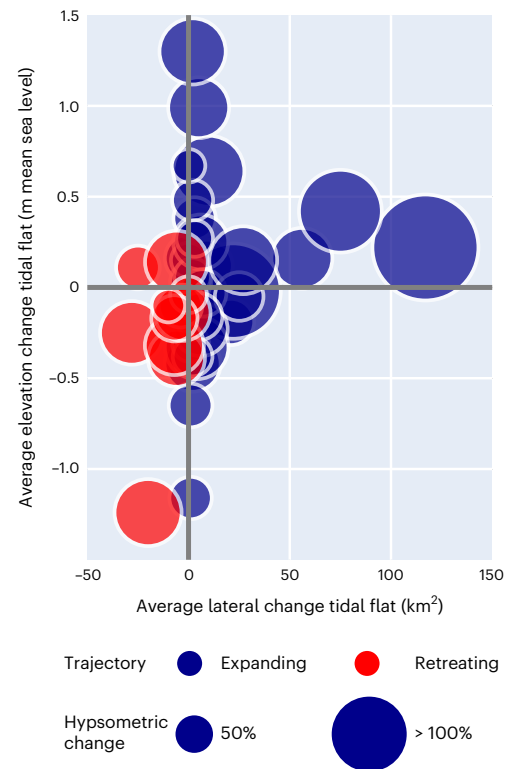


**Fig. 2 | Lateral versus vertical changes of the intertidal morphology between 1986–1988 and 2009–2011.** The morphology of tidal flats, both vegetated and unvegetated, can experience different trends in the different dimensions, for example, vertical erosion and lateral expansion.

extent (Fig. 1f). Overall, this negative trajectory could be due to a combination of factors such as net erosion caused by hydrodynamics (for example, changing wave climate, SLR, direct human interventions) and sediment supply changes<sup>19,21,30</sup>. Our analyses on a global scale show that lateral and vertical changes often occur simultaneously but not necessarily in the same direction (Fig. 2), such as vertical erosion coinciding with lateral expansion. These insights, derived from assessing changes in the hypsometric integral (HI), which quantifies sediment volume between mean low and high tides for both vegetated and unvegetated areas, add to previous research focusing primarily on lateral expansion globally<sup>18,23</sup>.

Understanding the morphological evolution requires consideration of the dynamics of vegetated intertidal areas (specifically, salt marshes and mangroves) as the sediment volume of these vegetated areas contributes to the sediment balance and dynamics of the intertidal zone<sup>38,39</sup>. In our assessment, 37.5% (15) of the estuaries experienced limited change within a range of –10% to +10% in the ratio of vegetated and unvegetated area, thus indicating relative stable conditions (Fig. 1g,h and Supplementary Table 1). Among the estuaries, 32.5% (13) had an increase in their vegetated tidal-flat proportion compared with the proportion unvegetated tidal flats (that is, negative ratios values in Fig. 1g,h), indicating more-persistent vegetated flats. Further, 30% (12) experienced a decrease in the proportion of vegetated tidal flats (that is, positive ratio values in Fig. 1g,h). For the 10 estuaries with negative tidal-flat trajectories, we found comparable trends: 30% (3) experienced stable vegetated versus unvegetated ratios. Further, 40% (4) showed a lesser retreat or even a gain in vegetated areas compared with unvegetated zones (see Supplementary Table 1). The other 30% (3), however, displayed similar or more-pronounced retreats in vegetated areas relative to unvegetated areas. These results indicate a variation in the ability of tidal flats to withstand environmental changes. Detailed process-based case studies are needed to understand the specific factors and dynamics at play in intertidal areas.

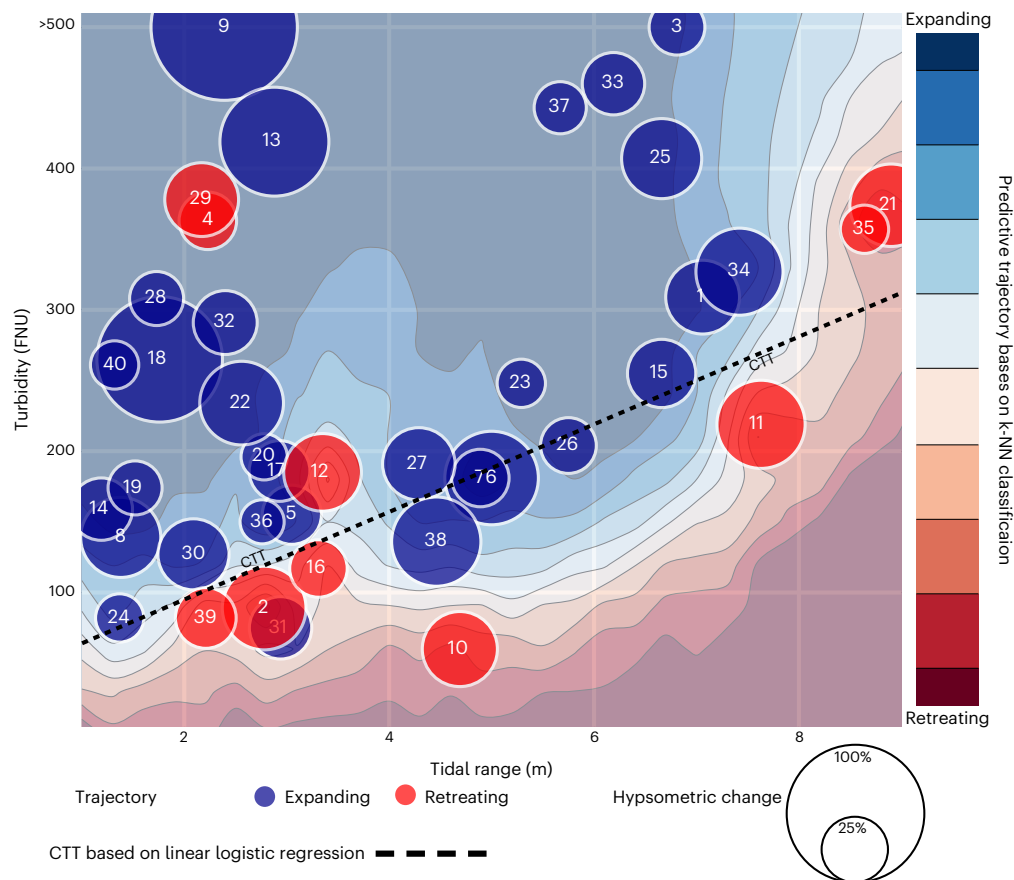


**Fig. 3 | The CTT to maintain intertidal areas worldwide based on supervised machine-learning techniques.** The predictive trajectory colours were estimated on the basis of supervised machine-learning k-NN classifications between retreating (red dots) and expanding (blue dots) tidal-flat trajectories, turbidity from 2009 to 2011 (FNU) and tidal ranges (m). The analysis indicates

that, in general, turbidity is critical in the development of tidal flats. The CTT (dotted line), derived from linear logistic regression, represents the minimum turbidity required to maintain estuarine tidal flats. Deviations around the line could be due to, for example, local environmental or anthropogenic factors.

### Impact of turbidity on tidal-flat morphology

The results show that the trajectory of tidal flats is closely associated with surpassing a CTT, which increases with tidal range (Fig. 3). Estuaries with high turbidity levels tend to exhibit expanding tidal flats in either a lateral or vertical dimension or in both dimensions. Conversely, estuaries in areas with low turbidity are more associated with retreat, and this becomes more evident in areas with higher tidal ranges (Fig. 3). This observation aligns with numerical models suggesting that a reduced tidal prism leads to increased sediment deposition on the shoals<sup>40</sup>, whereas estuaries with large tidal prisms face more frequent tidal erosion and thus require a higher sediment supply to prevent erosion. Our investigation into the persistence of tidal flats included turbidity (as a proxy for sediment supply) and tidal amplitude as key drivers of morphological changes. However, we also acknowledge that factors such as tidal currents and waves substantially impact the morphology<sup>28</sup>. We cannot directly include factors such as local tidal currents and waves in our analysis as they require global fine-scale and high-computation modelling or in situ measurement, which goes beyond the scope of remote sensing at global scales<sup>41,42</sup>. However, we assume that the impacts of these local hydrodynamic conditions are indirectly reflected in the tidal-flat morphology. Therefore, the deviations observed around the CTT are considered to encompass such influences indirectly.

The CTT can account for 84% of estuarine tidal-flat observed retreating and expanding trajectories. It signifies the critical lower boundary for tidal-flat sustainability; estuaries with turbidity levels falling below this threshold risk failing to maintain their current state and potentially disappearing. Of the estuaries studied, 75% (30) had

sufficient sediment availability to maintain or enhance their morphology (Fig. 3). The 25% (10) with negative trajectories experienced retreat in either one or both dimensions (Fig. 2). Notably, eight of these are in the Northern Hemisphere, where sediment supply reductions are more substantial<sup>31</sup>. Further, the negative trajectories imply that tidal flats facing future SLR-induced tidal amplification<sup>29,43</sup> (shifting from left to right in Fig. 3) may be at risk of loss (dropping below the CTT in Fig. 3) unless sediment supply increases. Therefore, to accurately predict the future trajectories of tidal flats, it is imperative to not only consider the influence of waves and tides<sup>28</sup> but also integrate the effects of tidal amplitude-dependent turbidity. Only 5% (2) of the estuaries deviated substantially from the expected CTT: the eroding Bahia Blanca and Mondego estuaries suffered notable anthropogenic modifications in the studied period. The Bahia Blanca Estuary (#4; Fig. 3) experienced a combination of SLR, interannual rainfall variations and human interventions during the measured period<sup>44</sup>, which caused its erosion to deviate from the trend substantially. The eroding Mondego Estuary (#29; Fig. 3) also suffered from many human interventions, including the construction of several dams and an artificial riverbed as well as water supply channels for agriculture, which caused substantial changes in the hydrological and sedimentary systems<sup>45,46</sup>.

In addition, we focused on the lateral expansion of either vegetated or unvegetated tidal flats if these indicators provide insight of the potential existence as well of a CTT (Extended Data Fig. 2). However, this approach alone did not reveal a CTT. It was only through examining changes in intertidal sediment volume by considering both vegetated

and unvegetated tidal flats together that we could identify a CTT. These results underscore the interconnectedness of vertical and horizontal changes in tidal flats and the link between vegetated and unvegetated areas. This highlights the importance of studying these habitats as an interconnected system to understand tidal-flat trajectories.

### Sediment supply key to maintain tidal flats

Present findings suggest the importance of sediment supply in maintaining tidal flats' elevations and extents, as affected by both dimensions; the CTT offers important implications for integrated estuarine management or modelling, particularly with accelerating SLR or human modifications. In the past, society may not always have adequately addressed the impact of sediment supply changes<sup>47,48</sup>, leading to the loss of ecological values. While a range of strategies is applied to maintain tidal flats, they are typically effective on a small and local scale and focus on hydrodynamics<sup>47</sup>. In scenarios of inadequate sediment supply to maintain estuarine tidal flats, the most effective solution might involve modifying or removing hard engineering structures such as dams, dykes and sea walls<sup>49</sup> as they substantially reduce sediment supply<sup>19,21,30,31,37</sup>. However, conducting targeted, local analyses to devise management strategies that comprehensively address all factors such as wave and tidal forcing, river discharge and thus sediment supply remains crucial.

### Online content

Any methods, additional references, Nature Portfolio reporting summaries, source data, extended data, supplementary information, acknowledgements, peer review information; details of author contributions and competing interests; and statements of data and code availability are available at <https://doi.org/10.1038/s41561-024-01431-3>.

### References

- Nicholls, R. J. et al. in *Climate Change 2007: Impacts, Adaptation and Vulnerability* (eds Parry, M. L. et al.) 315–356 (Cambridge Univ. Press, 2007).
- Kulp, S. A. & Strauss, B. H. New elevation data triple estimates of global vulnerability to sea-level rise and coastal flooding. *Nat. Commun.* **10**, 4844 (2019).
- Costanza, R. et al. The value of the world's ecosystem services and natural capital. *Nature* **387**, 253–260 (1997).
- Barbier, E. B. et al. The value of estuarine and coastal ecosystem services. *Ecol. Monogr.* **81**, 169–193 (2011).
- Reed, D., van Wesenbeeck, B., Herman, P. M. J. & Meselhe, E. Tidal flat–wetland systems as flood defenses: understanding biogeomorphic controls. *Estuar. Coast. Shelf Sci.* **213**, 269–282 (2018).
- Temmerman, S. et al. Ecosystem-based coastal defence in the face of global change. *Nature* **504**, 79–83 (2013).
- Zhu, Z. et al. Historic storms and the hidden value of coastal wetlands for nature-based flood defence. *Nat. Sustain* **3**, 853–862 (2020).
- Bouma, T. J. et al. Identifying knowledge gaps hampering application of intertidal habitats in coastal protection: opportunities & steps to take. *Coast. Eng.* **87**, 147–157 (2014).
- Menéndez, P., Losada, I. J., Torres-Ortega, S., Narayan, S. & Beck, M. W. The global flood protection benefits of mangroves. *Sci. Rep.* **10**, 4404 (2020).
- Kirwan, M. L., Temmerman, S., Skeehean, E. E., Guntenspergen, G. R. & Fagherazzi, S. Overestimation of marsh vulnerability to sea level rise. *Nat. Clim. Change* **6**, 253–260 (2016).
- Schuerch, M. et al. Future response of global coastal wetlands to sea level rise 1. *Nature* **561**, 231–234 (2018).
- Krauss, K. W. et al. How mangrove forests adjust to rising sea level. *N. Phytol.* **202**, 19–34 (2014).
- Mudd, S. M., D'Alpaos, A. & Morris, J. T. How does vegetation affect sedimentation on tidal marshes? Investigating particle capture and hydrodynamic controls on biologically mediated sedimentation. *J. Geophys. Res. Earth Surf.* **115**, F03029 (2010).
- Li, H. & Yang, S. L. Trapping effect of tidal marsh vegetation on suspended sediment, Yangtze delta. *J. Coast. Res.* **254**, 915–924 (2009).
- Bouma, T. J. et al. Short-term mudflat dynamics drive long-term cyclic salt marsh dynamics. *Limnol. Oceanogr.* **61**, 2261–2275 (2016).
- Hu, Z. et al. Mechanistic modeling of marsh seedling establishment provides a positive outlook for coastal wetland restoration under global climate change. *Geophys. Res. Lett.* **48**, 22 (2021).
- van Bijsterveldt, C. E. J. et al. Can cheniers protect mangroves along eroding coastlines? The effect of contrasting foreshore types on mangrove stability. *Ecol. Eng.* **187**, 106863 (2023).
- Murray, N. J. et al. The global distribution and trajectory of tidal flats. *Nature* **565**, 222–225 (2019).
- Syvitski, J. P. M. et al. Sinking deltas due to human activities. *Nat. Geosci.* **2**, 681–686 (2009).
- Dunn, F. E. & Minderhoud, P. S. J. Sedimentation strategies provide effective but limited mitigation of relative sea-level rise in the Mekong delta. *Commun. Earth Environ.* **3**, 2 (2022).
- Best, J. Anthropogenic stresses on the world's big rivers. *Nat. Geosci.* **12**, 7–21 (2019).
- Yang, S. L. et al. Role of delta-front erosion in sustaining salt marshes under sea-level rise and fluvial sediment decline. *Limnol. Oceanogr.* **65**, 1990–2009 (2020).
- Murray, N. J. et al. High-resolution global maps of tidal flat ecosystems from 1984 to 2019. *Sci. Data* **9**, 542 (2022).
- Bishop-Taylor, R., Sagar, S., Lymburner, L. & Beaman, R. J. Between the tides: modelling the elevation of Australia's exposed intertidal zone at continental scale. *Estuar. Coast Shelf Sci.* **223**, 115–128 (2019).
- Dogliotti, A. I., Ruddick, K. G., Nechad, B., Doxaran, D. & Knaeps, E. A single algorithm to retrieve turbidity from remotely-sensed data in all coastal and estuarine waters. *Remote Sens. Environ.* **156**, 157–168 (2015).
- Laengner, M. L., Siteur, K. & van der Wal, D. Trends in the seaward extent of saltmarshes across Europe from long-term satellite data. *Remote Sens.* **11**, 1653 (2019).
- Hayes, M. O. in *Geology and Engineering* (ed. Cronin, E. L.) 3–22 (Elsevier, 1975).
- Friedrichs, C. T. in *Treatise on Estuarine and Coastal Science* Vol. 3 (eds Wolanski, E. & McLusky, D.) 137–170 (Elsevier, 2012).
- Leuven, J. R. F. W., Pierik, H. J., van der Vegt, M., Bouma, T. J. & Kleinhans, M. G. Sea-level-rise-induced threats depend on the size of tide-influenced estuaries worldwide. *Nat. Clim. Change* **9**, 986–992 (2019).
- Syvitski, J. P. M., Vörösmarty, C. J., Kettner, A. J. & Green, P. Impact of humans on the flux of terrestrial sediment to the global coastal ocean. *Science* **308**, 376–380 (2005).
- Dethier, E. N., Renshaw, C. E. & Magilligan, F. J. Rapid changes to global river suspended sediment flux by humans. *Science* **376**, 1447–1452 (2022).
- Yang, S. et al. Storms dominate the erosion of the Yangtze delta and southward sediment transport. *Sci. Bull.* **68**, 553–556 (2023).
- Turner, R. E., Baustian, J. J., Swenson, E. M. & Spicer, J. S. Wetland sedimentation from hurricanes Katrina and Rita. *Science* **314**, 449–452 (2006).
- Gippel, C. J. Potential of turbidity monitoring for measuring the transport of suspended solids in streams. *Hydrol. Process.* **9**, 83–97 (1995).
- Zhu, C. et al. Properties of suspended sediment concentrations in the Yellow River delta based on observation. *Mar. Georesour. Geotechnol.* **36**, 139–149 (2018).

36. Grabemann, I., Uncles, R. J., Krause, G. & Stephens, J. A. Behaviour of turbidity maxima in the Tamar (U.K.) and Weser (F.R.G.) estuaries. *Estuar. Coast Shelf Sci.* **45**, 235–246 (1997).
37. Yang, S. L., Milliman, J. D., Li, P. & Xu, K. 50,000 dams later: erosion of the Yangtze River and its delta. *Glob. Planet. Change* **75**, 14–20 (2011).
38. Mariotti, G. & Fagherazzi, S. Critical width of tidal flats triggers marsh collapse in the absence of sea-level rise. *Proc. Natl Acad. Sci. USA* **110**, 5353–5356 (2013).
39. Fagherazzi, S. et al. Salt marsh dynamics in a period of accelerated sea level rise. *J. Geophys. Res. Earth Surf.* **125**, e2019JF005200 (2020).
40. Zhang, X., Fagherazzi, S., Leonardi, N. & Li, J. A positive feedback between sediment deposition and tidal prism may affect the morphodynamic evolution of tidal deltas. *J. Geophys. Res. Earth Surf.* **123**, 2767–2783 (2018).
41. Mao, Y., Harris, D. L., Xie, Z. & Phinn, S. Global coastal geomorphology—integrating Earth observation and geospatial data. *Remote Sens. Environ.* **278**, 113082 (2022).
42. Doherty, Y., Harley, M. D., Vos, K. & Splinter, K. D. A Python toolkit to monitor sandy shoreline change using high-resolution PlanetScope cubesats. *Environ. Model. Softw.* **157**, 105512 (2022).
43. Du, J. et al. Tidal response to sea-level rise in different types of estuaries: the importance of length, bathymetry, and geometry. *Geophys. Res. Lett.* **45**, 227–235 (2018).
44. Pralongo, P., Mazzon, C., Zapperi, G., Piovan, M. J. & Brinson, M. M. Land cover changes in tidal salt marshes of the Bahía Blanca estuary (Argentina) during the past 40 years. *Estuar. Coast Shelf Sci.* **133**, 23–31 (2013).
45. Cunha, P. P., Pinto, J. & Dinis, J. L. Evolução da fisiografia e ocupação antrópica na área estuarina do Rio Mondego e região envolvente (Portugal centro-oeste), desde 1947. *Territorium* **99**, 124 (1997).
46. Castro, P. & Freitas, H. Anthropogenic effects and salt marsh loss in the Mondego and Mira estuaries (Portugal). *Web Ecol.* **6**, 59–66 (2006).
47. Cox, J. R. et al. A global synthesis of the effectiveness of sedimentation-enhancing strategies for river deltas and estuaries. *Glob. Planet. Change* **214**, 103796 (2022).
48. Dunn, F. E. et al. Projections of declining fluvial sediment delivery to major deltas worldwide in response to climate change and anthropogenic stress. *Environ. Res. Lett.* **14**, 084034 (2019).
49. Bendixen, M., Best, J., Hackney, C. & Iversen, L. L. Time is running out for sand. *Nature* **571**, 29–31 (2019).

**Publisher's note** Springer Nature remains neutral with regard to jurisdictional claims in published maps and institutional affiliations.

Springer Nature or its licensor (e.g. a society or other partner) holds exclusive rights to this article under a publishing agreement with the author(s) or other rightsholder(s); author self-archiving of the accepted manuscript version of this article is solely governed by the terms of such publishing agreement and applicable law.

© The Author(s), under exclusive licence to Springer Nature Limited 2024

## Methods

### Classifying estuaries worldwide

Consistent DEMs of tidal flats worldwide were created using Landsat satellite data. This method employs the Google Earth Engine platform and the Geemap interactive mapping package in Python<sup>50–52</sup>. We employed atmospherically corrected US Geological Survey Landsat 5 surface reflectance tier 1 data, which includes a cloud and shadow mask that uses the CFMASK algorithm<sup>53</sup>. To identify estuaries with tidal flats and tidal vegetation, polygons were created via data from the Protected Planet database and Google Earth imagery<sup>54</sup>. We confined our analysis to specific sections or branches for particularly large estuaries, such as Anchorage, Chesapeake, Yangtze and Mekong (detailed shapefiles are available via the data availability statements). In addition, for estuaries with lengthy tidal rivers, such as Elbe, Fundy and Westerschelde, we excluded overly narrow parts. In this study, we used specific names accordingly. The remote-sensing analyses were conducted only on estuaries for which there were at least three consecutive years of satellite images in the periods 1986–1988 and 2009–2011 with a maximum of 60% cloud cover<sup>26</sup>.

We used an adapted version of the unsupervised salt-marsh classification procedure<sup>26</sup> that categorizes images into 3 yr periods in three groups: vegetation, unvegetated tidal flat and water. The 3 yr bins provided imagery that represented the entire range of tidal levels (Extended Data Fig. 3). We employed the normalized difference vegetation index and the normalized difference water index to classify each image in the 3 yr bins. Areas were classified as vegetation if they had a normalized difference vegetation index >0.3 and were classified as such for 80% of the time; these thresholds eliminate most of the temporal vegetation. Areas were classified as water if their normalized difference water index was greater than 0, and they were classified as such for 70% of the time. However, individual pixels were not classified as water if they had fewer than 150 adjacent pixels with water; this allowed us to correct for errors caused by the near-infrared band that could have been affected by white waters or high turbidity. The remaining pixels were classified as tidal flats.

### Tidal-range data

The tidal range was calculated using the worldtides.info application programming interface, which provides access to tidal data for tide stations worldwide<sup>55</sup>. We employed this application programming interface to retrieve a tidal height prediction relative to mean sea level for each image in the 3 yr bins by selecting the tidal station closest to the image's location. The limited number of available tidal stations restricted the number of estuaries that could be included in this study. We selected the most central station if multiple tidal stations were available. Further, we calculated the modelled tidal range as the difference between the average of all low waters and the average of all high waters recorded by the tidal station.

### Changes in vegetation coverage of intertidal surfaces

We quantified the changes in vegetated intertidal areas, particularly salt marshes and mangroves, by calculating the difference in percentage of intertidal areas that were vegetated in both the past and the present<sup>56</sup>.

$$\Delta V\% = \left( \frac{a_{v,i}}{a_{t,i}} \times 100 \right) - \left( \frac{a_{v,f}}{a_{t,f}} \times 100 \right) \quad (1)$$

In this equation,  $\Delta V\%$  is the resulting percentage of change in vegetated area  $a_v$  and the total vegetated and unvegetated intertidal area  $a_t$  in either the past (i) or the present (f). This method is an adaptation of the unvegetated/vegetated ratio<sup>57</sup>. By focusing on the proportion of the vegetated area within an intertidal environment, we can better understand the changes that have occurred in the intertidal zones, which provides valuable insights into morphological trajectories. Positive values indicate that the relative proportion of vegetated tidal flats declined, while negative values suggest a relative increase

in vegetated tidal flats, which implies a persistent ecosystem. Details of the vegetated and unvegetated areas ( $\text{km}^2$ ) in time are listed in Supplementary Table 1.

### Retrieving DEMs

We used the waterline extraction technique to create DEMs for the estuaries<sup>24</sup>. The 3 yr bin datasets were further divided into 10% intervals of the observed tidal height for each estuary. If more than two intervals contained no images, then we deleted the estuary from further analyses to avoid misinterpretations due to potentially dispersed data. The images in each interval were reprocessed according to the aforementioned described classification method to retrieve the waterline. With the `find_contours` function from `scikit.measure`<sup>58</sup>, we derived the waterline contours for each interval<sup>24</sup>. The median tidal height of the images in each interval was calculated and assigned to the extracted contour. After converting the contours to  $x$ -,  $y$ - and  $z$ -point data and combining all contours, we calculated continuous elevation data rasters using the `griddata` linear interpolation method from `scipy.interpolate`<sup>59</sup>. The final outcome of this process was  $30 \text{ m} \times 30 \text{ m}$  DEMs relative to the modelled mean sea level.

At the beginning of the assessment, we validated our method by testing the accuracy of the retrieved DEMs for the Westerschelde and Oosterschelde estuaries (the Netherlands), for which high-quality DEMs based on airborne lidar data were available. The results for the Westerschelde indicated a significant correlation with the lidar data, evidenced by the Pearson correlation coefficient of 0.83 and the Spearman correlation coefficient of 0.83, alongside a low root mean square error (RMSE) of  $\pm 0.50 \text{ m}$  (Extended Data Fig. 4). Similarly, the results for the Oosterschelde exhibited a strong correlation (Pearson correlation coefficient of 0.75 and Spearman correlation coefficient of 0.83) with an RMSE of  $\pm 0.45 \text{ m}$  (Extended Data Fig. 4). In both cases, the Pearson and Spearman correlations were highly significant, with  $P$  values less than 0.001. Next, we proceeded to acquire DEMs of tidal flats from various estuaries worldwide, particularly as uniform lidar or multibeam data are not commonly accessible worldwide.

During the analyses, we encountered challenges for estuaries located near the Equator (Amazon, Gulf of Nicoya Estuary and Muni-Pomadze Protected Area) due to the prevalent cloud cover in these regions. These estuaries were excluded from the analysis because they lacked images in at least 30% of the intervals, potentially leading to unreliable DEMs. In addition, high turbidity of the water led to an overassumption of tidal-flat area in a number of (upstream sections of) estuaries (Severn Estuary, Gironde Estuary and Humber Estuary), as judged visually; these estuaries were also excluded from analysis.

### Describing morphodynamic developments

Hypsometry measures the physical properties of an estuary's shape and structure<sup>60</sup> and transforms the cumulative frequency distribution of a tidal flat's bed-level elevation into a single line. Hence, changes in the shape of a hypsometric curve can provide insight into an estuary's morphological development. In this study, intertidal hypsometric curves are defined as the cumulative frequency distribution of elevations, where the  $y$  axis represents the percentage of the tidal flat area between the low and high tide and the  $x$  axis represents the extent itself.

$$H(y) = A(y)/A \quad (2)$$

In this equation,  $H(y)$  is the cumulative frequency distribution of elevations up to elevation  $y$ ,  $A(y)$  is the area of the tidal flat below elevation  $y$  and  $A$  is the total area of the tidal flat (Extended Data Fig. 3). As we studied the morphological trajectory, we employed a hypsometric curve to describe the past (1986–1988) and the present (2009–2011). For the comparison,  $A$  is the maximum cumulative area in time, regardless of whether the time is past or present. In addition, we wanted to ensure an accurate interpretation of the hypsometric curve and account for the influence of potential vegetated tidal-flat expansion

or retreat, so we incorporated the vegetated tidal-flat extent into the hypsometric plot (Extended Data Fig. 3). Specifically, we assigned the highest measured water level as the elevation of the vegetated tidal flat. Further, we limited the  $y$  range as the issue of offset could occur if the Landsat images of both periods do not cover the same tidal range (Extended Data Fig. 3). To overcome this, we created high- and low-water boundaries for the hypsometric curve that were defined by taking the maximum and minimum values for the low and high tides, respectively, measured between the two periods (Extended Data Fig. 3). This approach ensured that the entire range of tidal elevations was captured and considered in the analysis while minimizing potential biases in the dataset. We compared the modelled tidal range with the observed tidal range used in the hypsometric curves. Overall, satisfactory agreement was noted, indicating that the method reflected the tidal-flat extent (Extended Data Fig. 5).

After we created the cumulative frequency distribution of elevations, we fitted either a second- or third-order polynomial function to independently describe the hypsometric curve for each estuary (Supplementary Table 1)<sup>61</sup>. On the basis of the intertidal hypsometric curves, we calculated the HI, which is an index that describes an estuary's topography on the basis of the hypsometry and is unaffected by the slope or aspect over space<sup>61</sup>. In our case, the HI described the intertidal volume of sediment. The HI is a dimensionless number between 0 and 1, which enabled us to compare the hypsometric curves between estuaries and periods regardless of differences in scale, such as tidal range, extent and elevation<sup>60</sup>. We calculated the percentage difference in HIs between the periods to identify the morphological trajectories (Supplementary Table 1). A gradually increasing HI indicates that the amount of sediment in the intertidal range increased, while a decreasing HI indicates a decline of sediment.

For the unvegetated tidal flats, we calculated the average difference between the  $x$  values of the periods for 100 points integrated over the second- or third-order polynomial regressions as well as the average change in elevation. The average difference indicated whether changes in sediment volume typically occurred laterally or vertically. In other words, the average difference between the hypsometric curves indicated whether the tidal flats experienced development in either a lateral or vertical direction.

### Turbidity for estuaries

Obtaining accurate measurements of suspended sediment concentrations (SSCs) through in situ measurements or remote sensing with region-specific calibration can be challenging and may limit the application of SSCs on a global scale. However, turbidity is often used as a proxy for SSC<sup>25,34,62</sup> and can be easily and globally retrieved through remote sensing using a single algorithm that provides measurements in the 1–1,000 FNU range<sup>25</sup>. We deployed this existing semi-analytical turbidity algorithm for the red and near-infrared bands for the US Geological Survey Landsat 5 surface reflectance tier 1 dataset. The near-infrared band retrieves turbidity levels in highly turbid waters, while the red band performs better in calculating concentrations in medium- to low-turbidity waters. While the semi-empirical algorithm effectively estimates turbidity across diverse regions, it is important to note the associated uncertainties due to varying particle types, bidirectional effects and non-linear responses<sup>25</sup>. Consequently, the algorithm was applied to each image within the 3 yr period, with the median turbidity calculated for each image. From these median values, we derived the average turbidity for the entire 3 yr period. Further, the dataset was tested for dispersion to avoid skewness in the dataset (for example, measuring during only high tides or summer conditions; see Supplementary Table 1).

The dispersion indexes for time and water level were calculated for each image in the 3 yr bin for either the past or present. The dispersion index is a ratio of the variance from the mean of either time or water level, which allowed us to identify whether the 3 yr bin was skewed or

biased for one of the classes. A value close to 1 indicates that the data are spread across the temporal scale and elevations, meaning that no clusters impact the data; in other words, the data are well distributed over time, water levels and tidal cycles. For data integrity, we set boundary conditions: estuaries with an index value below 0.7 for both time and water level in any 3 yr bin would be considered unsuitable due to potential clustering and removed from our analysis. Similarly, a threshold of 0.5 for a single class (for example, time or water level) in a 3 yr bin was set for exclusion due to data clustering. The boundary conditions resulted in not all estuaries being suitable for analysis globally (Ashepoo Combahee Edisto Basin National Estuarine and Bubiyan Island).

To determine whether there were significant differences ( $P < 0.05$ ) in turbidity between the first and last periods, we used two-sample  $t$  tests to compare the concentrations measured for each image in the 3 yr bins. Since a range of temporal factors can influence turbidity, we compared the first and last groups of our data instead of examining temporal trends. We calculated median turbidity per 3 yr group, which was used for further data analyses.

### Assessing the critical turbidity limit

Before we assessed the CTT, we assumed and set manually that tidal flats could not exist with a turbidity of 0 FNU (ref. 63). We employed a linear logistic regression to model the relationship among the tidal range, turbidity and morphological trajectory of the tidal flat. Our goal was to identify the linear function that optimally differentiated between expanding and retreating morphological trajectories. With the LogisticRegression function from `sklearn.linear_model`<sup>58</sup>, we derived the CTT—the boundary between retreating and expanding tidal flats. The quality of the derived linear regression was tested with the `sklearn.linear_model` package<sup>58</sup>; results indicated that the CTT can explain 84% of the measured morphological trajectories.

To improve the visualization of the findings, we also employed the  $k$ -nearest neighbour ( $k$ -NN) classification method from `sklearn.neighbors` package<sup>58</sup>, a non-parametric approach, rather than a linear logistic regression. The  $k$ -NN method estimates a new observation's value on the basis of its  $k$ -NN values. Both methods are machine-learning techniques that allow researchers to make predictions, whereas the linear logistic regression provides a decision boundary. The presented results for the  $k$ -NN and CTT visualize the transition from tidal-flat retreat to expansion in a similar area (Fig. 2).

### Data availability

All datasets used in this study are publicly available. The satellite imagery is freely available via the Google Earth Engine Catalog. The tidal data, including satellite telemetry and gauge data, can be accessed from WorldTides (<https://www.worldtides.info/apidocs>). The original shapefiles for the presented estuaries can be downloaded from Protected Planet (<https://www.protectedplanet.net/>) and are archived on Zenodo with respect to the presented study (<https://doi.org/10.5281/zenodo.8172387>)<sup>64</sup>. Data used for Figs. 1–3, as well as Extended Data Figs. 1, 2 and 5, are provided in Supplementary Table 1. Data used for Extended Data Figs. 3 and 4 are available at <https://doi.org/10.5281/zenodo.8172387>. The basemap world imagery of Fig. 1 is sourced from Esri, Maxar, Earthstar Geographics and the GIS User Community available at [http://goto.arcgisonline.com/maps/World\\_Imagery](http://goto.arcgisonline.com/maps/World_Imagery).

### Code availability

The code was developed in Python version 3.11.0. The code for retrieving digital elevation models per estuary, extracting turbidity concentration, computing the hypsometric integral (Extended Data Fig. 1) and quantifying the dispersion index has been archived and is publicly available via Zenodo at <https://doi.org/10.5281/zenodo.8172387> (ref. 64). This repository also contains the code and data used for validating the modelled intertidal DEMs, as seen in Extended Data Fig. 3.

## References

50. Wu, Q. geemap: a Python package for interactive mapping with Google Earth Engine. *J. Open Source Softw.* **5**, 2305 (2020).
51. Wu, Q. et al. Integrating LiDAR data and multi-temporal aerial imagery to map wetland inundation dynamics using Google Earth Engine. *Remote Sens. Environ.* **228**, 1–13 (2019).
52. Gorelick, N. et al. Google Earth Engine: planetary-scale geospatial analysis for everyone. *Remote Sens. Environ.* **202**, 18–27 (2017).
53. Foga, S. et al. Cloud detection algorithm comparison and validation for operational Landsat data products. *Remote Sens. Environ.* **194**, 379–390 (2017).
54. *Protected Planet: The World Database on Protected Areas (WDPA)* (UNEP-WCMC & IUCN, 2023); [www.protectedplanet.net](http://www.protectedplanet.net)
55. *Worldwide Ocean and Sea Tide Predictions* (Worldtides, 2023); [Worldtides.info](http://Worldtides.info)
56. Wasson, K. et al. Understanding tidal marsh trajectories: evaluation of multiple indicators of marsh persistence. *Environ. Res. Lett.* **14**, 124073 (2019).
57. Ganju, N. K. et al. Spatially integrative metrics reveal hidden vulnerability of microtidal salt marshes. *Nat. Commun.* **8**, 14156 (2017).
58. Pedregosa, F. et al. Scikit-learn: machine learning in Python. *J. Mach. Learn. Res.* **12**, 2825–2830 (2011).
59. Virtanen, P. et al. SciPy 1.0: fundamental algorithms for scientific computing in Python. *Nat. Methods* **17**, 261–272 (2020).
60. Strahler, A. N. Hypsometric (area-altitude) analysis of erosional topography. *Geol. Soc. Am. Bull.* **63**, 1117–1142 (1952).
61. Harlin, J. M. Statistical moments of the hypsometric curve and its density function. *J. Int. Assoc. Math. Geol.* **10**, 59–72 (1978).
62. Ralston, D. K., Yellen, B., Woodruff, J. D. & Fernald, S. Turbidity hysteresis in an estuary and tidal river following an extreme discharge event. *Geophys. Res. Lett.* **47**, 15 (2020).
63. Gao, S. in *Coastal Wetlands* (eds Perillo, G. M. E. et al.) 359–381 (Elsevier, 2019).
64. Grandjean, T. J. et al. Data, scripts underlying the publication: identifying the critical turbidity threshold to maintain estuarine tidal flats worldwide. *Zenodo* <https://doi.org/10.5281/zenodo.8172387> (2023).

## Acknowledgements

This work was supported by the Royal Netherlands Academy of Arts and Sciences (KNAW) (grant PSA-SA-E-02).

## Author contributions

T.J.G. and T.J.B. conceived the idea. T.J.G. and R.W. developed the methodology and performed the analyses of the results. D.v.d.W., E.A.A., Z.H., Z.B.W. and T.J.B. contributed to the methodological improvement in data analysis. T.J.G., R.W., D.v.d.W., E.A.A., Z.H., S.L., Z.B.W., Y.L. and T.J.B. contributed to the paper writing, editing and conceptualization and agreed with the final version.

## Competing interests

The authors declare no competing interests.

## Additional information

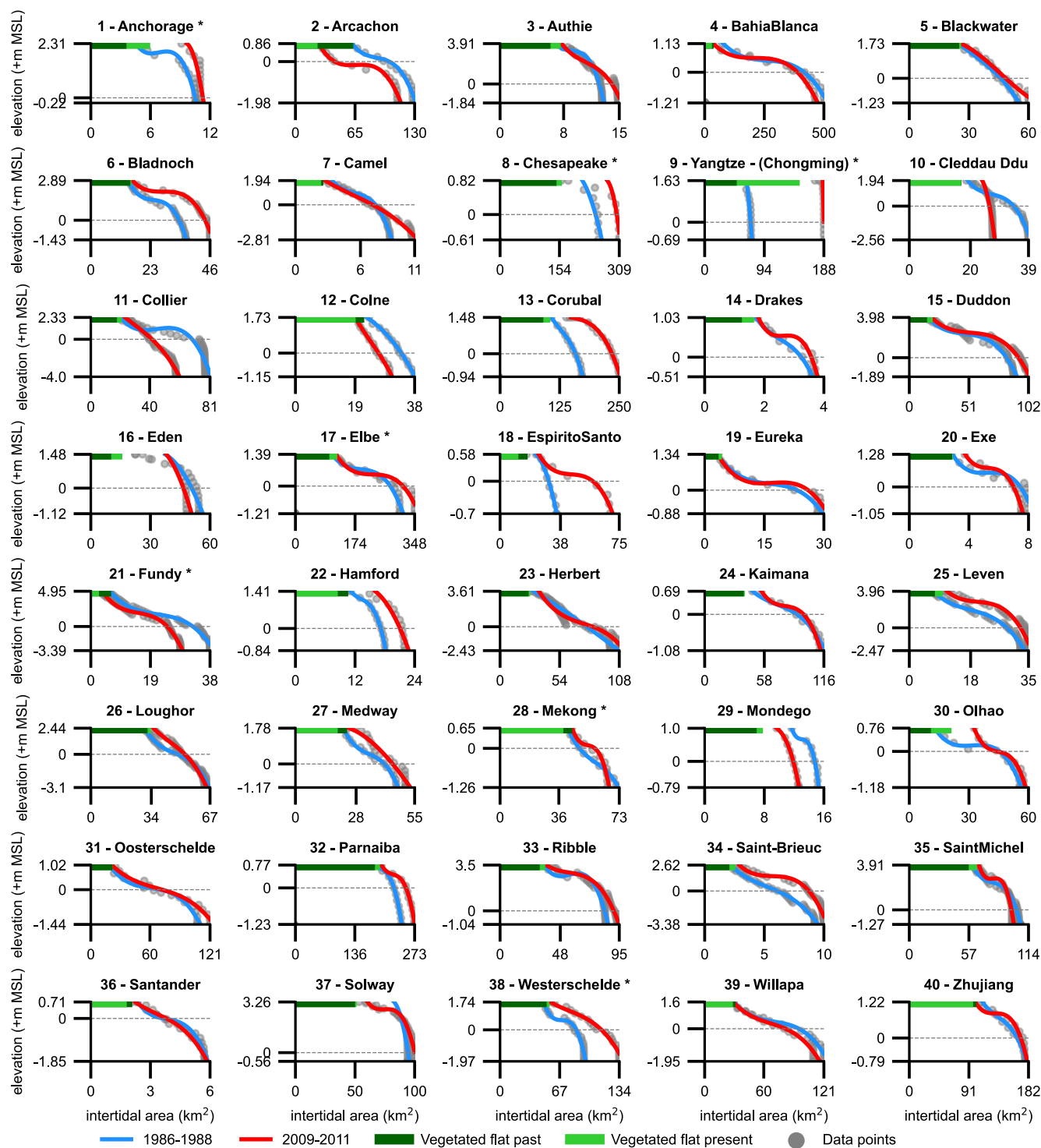
**Extended data** is available for this paper at <https://doi.org/10.1038/s41561-024-01431-3>.

**Supplementary information** The online version contains supplementary material available at <https://doi.org/10.1038/s41561-024-01431-3>.

**Correspondence and requests for materials** should be addressed to Tim J. Grandjean.

**Peer review information** *Nature Geoscience* thanks Stuart Phinn and the other, anonymous, reviewer(s) for their contribution to the peer review of this work. Primary Handling Editor: Tamara Goldin, in collaboration with the *Nature Geoscience* team.

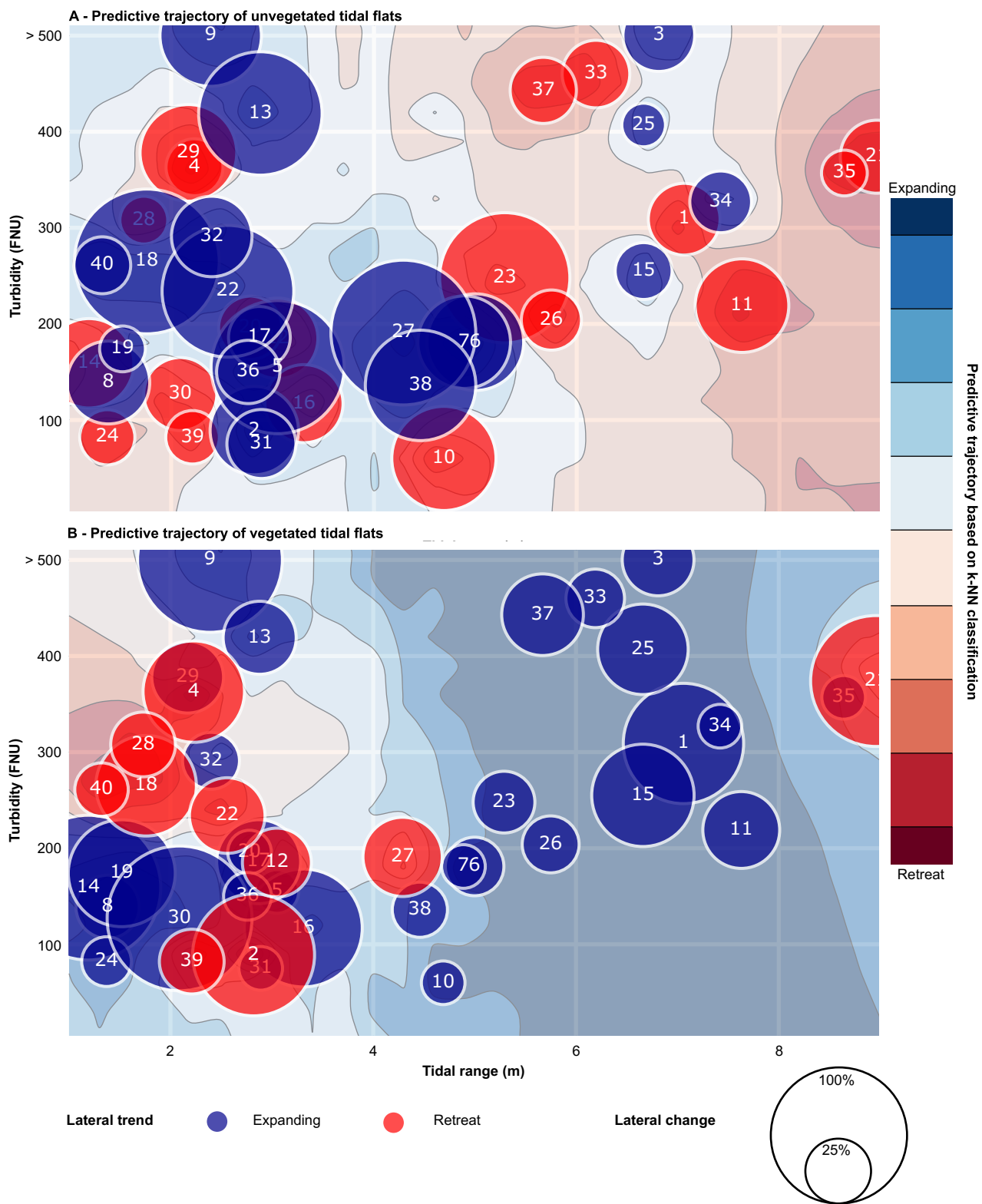
**Reprints and permissions information** is available at [www.nature.com/reprints](http://www.nature.com/reprints).



\* part of the estuary

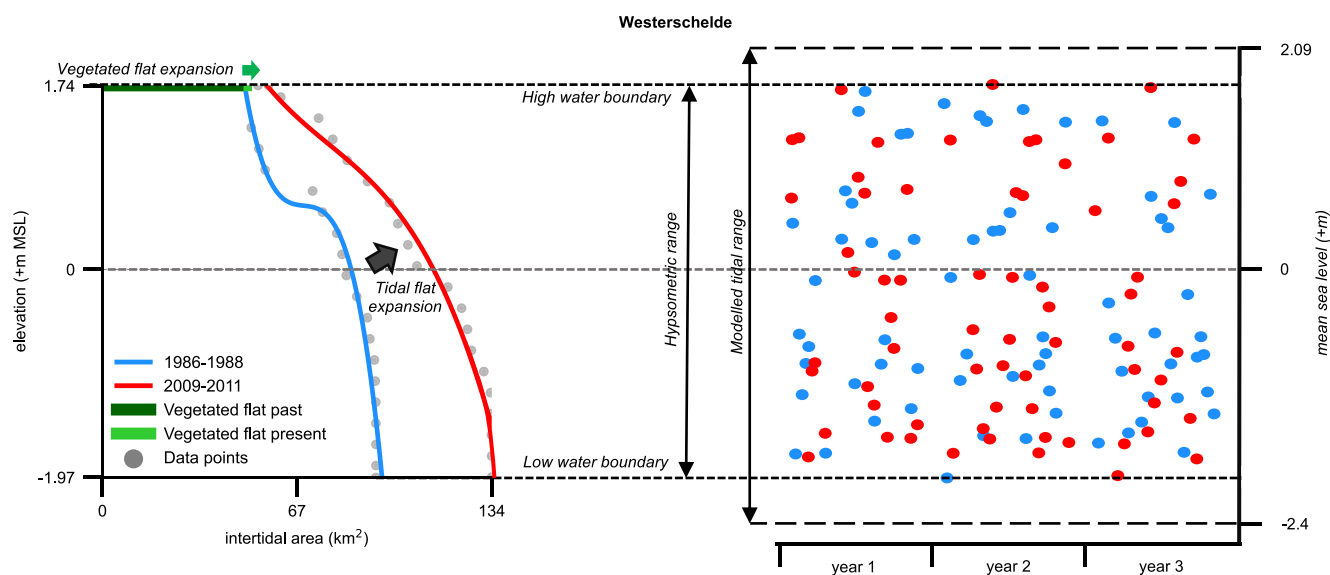
**Extended Data Fig. 1 | Hypsometric curves comparing past and present tidal flat morphologies for 40 estuaries globally.** The hypsometric curves illustrate the tidal flat morphologies for 1986–1988 (past, blue line) and 2009–2011 (present, red line). The lines represent second- or third-order polynomial regressions, fitted through the data points (grey points) for the respective period. The data points are calculated from the generated DEMs and represent the intertidal area (x-axis) above the corresponding elevation (y-axis). All satellite images used to generate the DEM are within the elevation range, called

the hypsometric range (as detailed in Extended Data Fig. 3). The vegetated tidal flat (green line), salt marsh or mangrove is part of the analyses and bound to the maximum observed elevation. Some estuaries were partly studied (\*) as their extent was too large for the available computational powers. Details regarding the retrieval of this figure can be found in the methodology section ‘Describing morphodynamic developments’ and Extended Data Fig. 3. Details regarding the  $R^2$  and the order used for each hypsometric curve can be found in Supplementary Table 1.



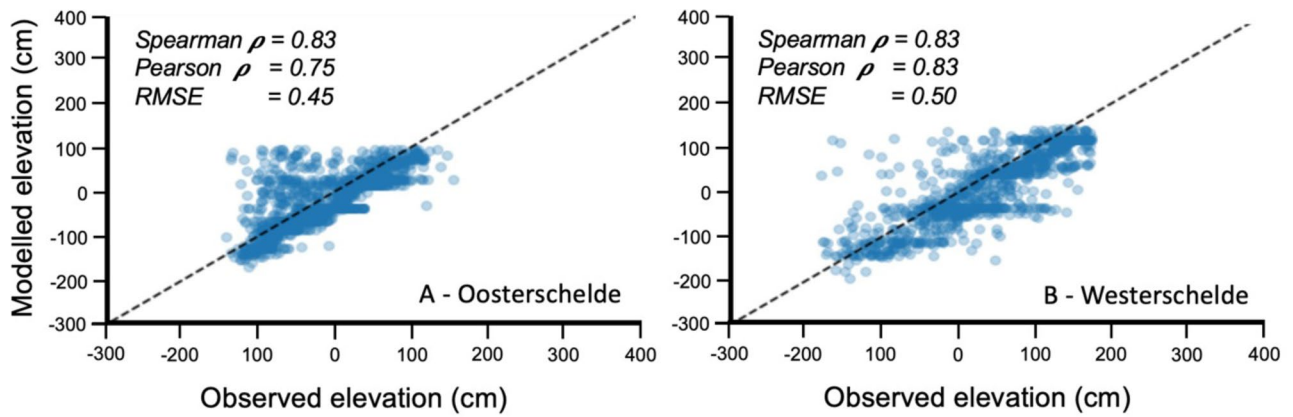
**Extended Data Fig. 2 | Lateral trends in (A) unvegetated tidal flats and (B) vegetated tidal flats as a function of turbidity and tidal range.** The results show a random pattern; there is no predictive trajectory of lateral trends present for the supervised machine learning k-NN classification between retreating (red

dots) and expanding (blue dots) lateral trends for either (A) unvegetated tidal flats or (B) vegetated tidal flats. To study morphological trajectories, it appears important to consider both the vegetated and unvegetated intertidal areas in a multi-dimensional aspect (see Fig. 3 of main article).



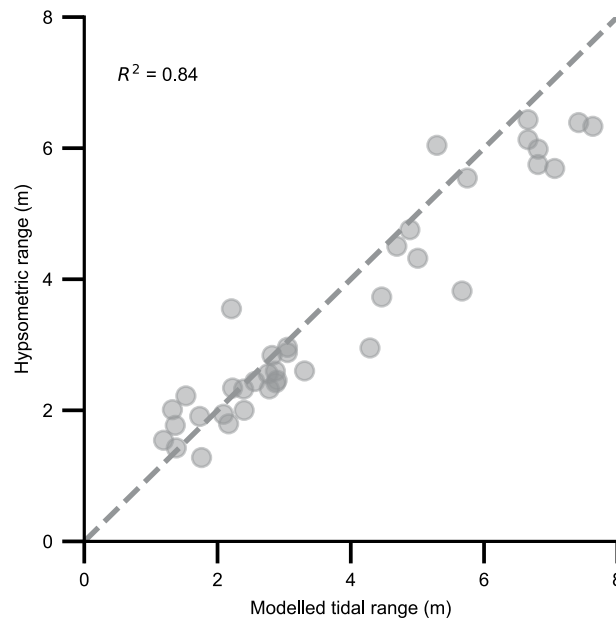
**Extended Data Fig. 3 | Example of the retrieval of the hypsometric range from the distribution of Landsat images per three-year bin relative to each other for the Westerschelde estuary (the Netherlands).** The hypsometric curve in this figure was generated using a DEM obtained through a waterline extraction method. The analyses were based on three years of data for each curve and represent the proportion of the tidal basin height in relation to the lowest maximum water level (high-water boundary) and the highest minimum water level (low-water boundary) observed within both periods. It is important

to note that the tidal range can exceed the hypsometric range represented by the hypsometric curve. The vegetated tidal flat extent was incorporated in the hypsometric. Vegetated tidal flats are an integral component of an estuary's intertidal environment; hence, they were incorporated into the tidal basin area at the high-water boundary. The data represented in the right plot is as well used for calculating the dispersion index. Should we observe clustering within a three-year bin, the data points would exhibit skewness. This could occur either on the vertical axis, reflecting the mean sea level, or along the time-oriented x-axis.



**Extended Data Fig. 4 | Validation results for the modelled intertidal DEMs.** The retrieved DEMs for (A) Oosterschelde and (B) Westerschelde estuaries in the Netherlands were compared with airborne LiDAR data, which was corrected

to MSL. The Spearman and Pearson correlation coefficients ( $\rho$ ) and the RMSE were calculated to test the resemblance. In both cases, the Pearson and Spearman correlations were highly significant, with p-values less than 0.001.



**Extended Data Fig. 5 | Comparison of the modelled tidal and observed hypsometric ranges.** This figure compares each estuary's average tidal range at a central or nearby tidal station with the hypsometric range observed. The results show a high degree of determination ( $R^2 = 0.84$ ) between the hypsometric and

tidal ranges, suggesting that the DEM accurately reflects the extent of the tidal flats. However, a slight discrepancy exists in areas with a higher tidal range ( $>4$  m) due to limitations of the remote sensing data acquisition to capture the full range from low to high water levels.